



Choking dynamic of highly swirled flow in variable nozzle radial turbines



Andrés Tiseira^a, Vicente Dolz^a, Lukas Benjamin Inhestern^b, Juan David Echavarría^{a,*}

^a CMT-Motores Térmicos, Universitat Politècnica de València, Camino de Vera, 46022 València, Spain

^b Institute of Aeronautics and Astronautics, TU Berlin, Marchstraße 12-14, 10587 Berlin, Germany

ARTICLE INFO

Article history:

Received 11 January 2021

Received in revised form 5 January 2022

Accepted 28 January 2022

Available online 31 January 2022

Communicated by Kivanc Ekici

Keywords:

Aerodynamics

Radial turbine

Shock waves

Choking

Rotor-stator interaction

CFD

ABSTRACT

This paper presents the results of a computational investigation of the aerodynamic choking mechanism in a variable geometry turbine, which is widely used in automotive turbocharging. RANS and URANS numerical simulations were carried out for two stator vane positions, 10% and 30% opening at different speeds and several other operating conditions to observe the establishment of choked flow and rotor-stator interactions. When the stator vanes are at a closed position and high-pressure ratio, a shock wave is developed on the suction side of the stator vane; moreover, the effective area extends toward the rotor inlet. The shock losses of a fluid particle upstream of the rotor are related to the number of shocks that the particle goes through. The pressure losses are high close to the stator vanes and start to decrease toward the center of the vaneless space until they start to increase close to the rotor. The interaction between the rotor and stator creates shock waves with an intensity depending on the rotor's leading edge position and the rotational speed. The pressure profile of the rotor blade under this circumstance is also affected, especially at high rotational speeds, when important load fluctuations may affect the integrity of the blades.

© 2022 The Authors. Published by Elsevier Masson SAS. This is an open access article under the CC BY-NC-ND license (<http://creativecommons.org/licenses/by-nc-nd/4.0/>).

1. Introduction

In the turbocharger market, manufacturers continuously push to develop turbos with higher efficiency over a broader range of pressure ratios and large capacity over a wide operating range [1,2]. Turbochargers are commonly used for energy recovery in complex systems and can widely be found in the automotive sector as well as in the commercial aircraft industry [3]. In a commercial airplane, the turbocharger can be found in new technologies that are an alternative to the traditional gas turbine auxiliary power units (GTAPUs) [4] or may be part of the environmental control system (ECS) [5] having different configurations, one of them is used to convert the energy of the cabin discharged air into mechanical energy and pre-supercharge the fresh air for reducing the electrical power required by the electrically driven ECS [6]. Transforming the traditional bleed engine style for the ECS to the electrically driven one, turbochargers can reduce the input power and increase the coefficient of performance (COP) [7]. In the automotive sector, the turbochargers with the variable geometry turbines (VGTs) have been widely applied to improve the operation of the engine at low speed-torque, and the transient response [8,9]. Aside

from the advantages mentioned above, other key aspects are overboosting prevention, engine downsizing, and better fuel economy [10–13]. The operation principle of the VGT is based on the position change of the stator vanes to alter the nozzle geometry reducing or increasing the exhaust gas velocity upstream of the rotor [14]. When a VGT works with rather closed nozzle vanes, as is the case during sudden internal combustion engine (ICE) accelerations, the turbine works with high-pressure ratios. Under these conditions, the turbine may choke, and shock waves generate important losses. The shock can be located between the stator vanes throat and trailing edge area [15,16]. The interaction among shock, leakage flow, and nozzle wake affect the unsteady flow and blade loads. Therefore it is necessary to investigate this interaction to understand the underlying mechanism contributing to the change in the flow characteristics [17,18] to design an optimal turbine that provides the maximal efficiency [19]. Liu et al. [20] found that the strong nozzle leakage flow weakens the shock strength at the nozzle trailing edge and affects the inlet flow angle distribution of the rotor blade, and increases the rotor blade aerodynamic losses. Chen [21] highlights that the exhaust gases of diesel engines at low speed can lead to a shock impinging on downstream rotor blades affecting the integrity of the turbine; moreover, the nozzle clearance leakage flow increases flow unsteadiness inside the passage of the turbine wheel and leads to a significant increase of turbine

* Corresponding author.

E-mail address: juaecol@mot.upv.es (J.D. Echavarría).

Nomenclature

Notations

Ma	Mach Number
\dot{m}	Mass Flow
$\dot{m}_{red.}$	Reduced Mass Flow
p	Pressure
r	Radius
T	Temperature or Period
t	Time
N	Rotational speed
\dot{W}	Power

Abbreviations

BSR	Blade speed ratio
CFD	Computational Fluid Dynamics
SS	Suction Side
PS	Pressure Side

RANS	Reynolds Average Navier Stokes
URANS	Unsteady Reynolds Average Navier Stokes
VGT	Variable Geometry Turbine

Greek symbols

α	Stator Blade Angle
η	Efficiency
π	Corresponding Pressure Ratio

Subscripts

in	Turbine Inlet Section
$red.$	Reduced Numbers
$rel.$	Relative Value
s	Static Conditions
$surf.$	Stator Vane or Rotor Blade Surface
tot	Total or Stagnation Conditions
t, s	Total-To-Static Value

vibration stress [22,23]. Similar results were obtained by the investigation of Shi et al. [24] about the effects of the nozzle vanes clearance leakages, wake and shock wave on the rotor blade pressure fluctuations, showing that the shock wave and nozzle vanes clearance leakages are the main reason for the fluctuations; moreover, the pressure response on the suction surface of the blade near leading edge is mainly influenced by the shock wave. The unsteady, pulsating flow is responsible for a complex flow field in the radial turbine [25–27]. According to Qi et al. [28] the inlet pulsating flow influences the clearance leakage flow and the shock wave position, shifting the shock wave downstream of the nozzle trailing edge. In addition to that, the inlet pulsating flow influences the separation caused by the incidence angle at the rotor inlet, thus decreasing the turbine efficiency. Furthermore, based on the results of Xue et al. [29] the secondary flow is the main source of flow loss in the nozzle under pulsating flow conditions, but this loss is lower under quasi-steady conditions. Regarding the effect on the rotor, Paniagua et al. [30] analyzed the stator-rotor interaction in highly loaded high-pressure turbines finding that the vane shock impingement on the rotor generates a separation bubble on the rotor that is responsible for the generation of high losses. The increase of static pressure and heat flux fluctuations results from the more intensive vane trailing edge direct shock and reflected shock impacting the rotor. The stator vanes thickness, solidity, and number are other important aspects related to the shock and rotor load. Yang et al. [15] found that thickness and number of stator vanes affect the intensity of the shock in the vaneless space. When increasing the vane number and the solidity, the intensity of the shock decreases around 75%, moreover at 50% span, the shock changes in shape and strength due to the impact of the relative position between rotor and stator. Regarding the load, the spikes appear at the rotor trailing edge, and its magnitude and the fluctuation amplitude decrease when the blade number increases. Similar results were obtained by Hayami et al. [31]. Simpson et al. [32] found that increasing the values of both the solidity and the distance between vane trailing edge and rotor trailing edge lead to a reduction in the amplitudes of the measured and predicted static pressure variations at the rotor inlet, besides being more aerodynamically efficient to achieve a circumferential uniform flow state around the rotor periphery.

Studying the flow field in the vaneless space, the interaction of the nozzle leakage flow with the main flow, the flow losses, and conditions of the incoming flow to the rotor is important to improve the energy extraction from the exhaust gas. This is the

reason why several investigations have been focused on this region. According to Qiu et al. [33] the nozzle clearance carries a portion of the flow that is not turned by the nozzle vanes and has a high radial velocity and a small swirl which influence the power output and the turbine efficiency; moreover, the choking limit of the nozzle is also increased because of the presence of the clearance. Sato et al. [34] conducted unsteady CFD and experimental analyses to investigate the effects of rotor-stator interaction on the rotor excitation forces, concluding that at stator vanes closed position, the effect of shock waves on the excitation force is intensified when increasing the pressure ratio and Mach number. These results suggest that excitation force can be calculated using the dynamic pressure and Mach number at the rotor inlet in a one-dimensional model. Yang et al. [35] perform numerical simulations to study the generation and weakening mechanism of the shock wave in VGTs. The shock waves at the vane trailing edge vary in intensity and shape when the distance between the vanes and rotor blade changes; moreover, the shrinkage degree between the stator vane trailing edge and the rotor blade can weaken the trailing edge shock wave and thus, reduce the pressure fluctuations on the rotor blade leading to high cycle fatigue. According to Liu et al. [36] the pressure fluctuation level is three times the subsonic condition at transonic conditions. Several studies, such as those by Simpson et al. [37,38] and Spence et al. [39] have analyzed the flow structure and losses in the volute and stator.

However, few studies are focusing on shock related loss generation in the vaneless space, one of them is the design method proposed by Chen et al. [40] with the aim to reduce the shock loss and shockwaves in the vaneless space of turbochargers turbines with VGT by making the suction surface of the vane flatter. Furthermore, there are relatively few studies about the swirled flow in the vaneless space of radial turbines. One of them is the experimental study carried out by Fontaneto et al. [41] using Particle Image Velocimetry (PIV) and micro cylindrical pressure probes to describe the strongly swirling flow field whose tangential velocity increases downstream. The swirl flow is mainly highlighted on the one hand at the inlet of the nozzle due to the strong nature of the flow discharging from the engines affecting the power output [42–44]. On the other hand, the minimum adverse flow-swirl at the turbine outlet is evaluated to obtain an optimum blade outlet angle during the development of loss models [45] or analyzed through experimental LDV (Laser Doppler Velocimeter) to validate CFD results [46]. Thus, this study contributes to the analysis of the

swirled flow considering the vaneless space of the radial turbine reaching sonic conditions.

In an automotive VGT, a wide variety of operating conditions at different VGT positions and rotational speeds increase the complexity of the choking behavior. The current extensive investigation has been conducted to give new insights, where choked flow in the vaneless space and the effects on the rotor blade surface are studied at numerous working conditions. Computational fluid dynamic (CFD) simulations are conducted to obtain and analyze the aerodynamic features under choking conditions. This work is divided into the following parts: First, a description of the turbine geometry and setup used for the steady and unsteady simulations with different stator vane openings, pressure ratios, and rotational speed is presented. Second, the simulation results, streamlines and cylindrical sections on the vaneless space, and the unsteady rotor-stator interaction are presented and interpreted. The discussion and conclusions of the obtained results form the final part of this paper.

2. Geometry description

A radial turbine with a variable nozzle used in automotive turbochargers was taken for this study. To be more specific, this turbocharger can be found in Sport Utility Vehicles (SUVs) with a diesel engine of 1995 cm³, four cylinders, a maximum power out of 110 kW at 4000 rpm, and a maximum torque of 320 N m at 2000 rpm. Two nozzle vane openings corresponding to 10% and 30% VGT opening were considered because when the turbine operates with high inlet pressure and small nozzle opening, a shock wave may appear on the vanes [47,48]. Furthermore, the opening position of 10% VGT was selected by Tiseira et al. [16] to analyze the internal flow at off-design conditions reaching choked flow. Thus, to analyze deeper the establishment of choked flow and the rotor-stator interaction, this position was selected together with 30% VGT opening, which the control system of the engine can set at full load or load acceptance transient (sudden tip-in) test [2,49–51]. The same geometry was investigated with the same vane openings at high blade speed ratios by Serrano et al. [52]. The turbocharger was experimentally assessed by Serrano et al. [53] and previously achieved data will be used as a validation basis in this paper. The most important dimensions of the stator and rotor are listed in Table 1, while Fig. 1 depicts the selected stator vane openings. The maximum aperture of the vanes allowed by the mechanism that controls their position is presented in Table 1 and denoted as 100% VGT to put in context the selected openings of 10% VGT and 30% VGT. The fluid domain consists of the inner volume of the inlet duct, volute, stator, rotor, and outlet duct. The inlet duct has a length of six duct diameters, and the outlet duct has a length of nine duct diameters. To have a static pressure in the outlet of the computational domain similar to the static pressure close to the rotor outlet, the outlet pipe has a convergent duct with an exit diameter equal to the rotor outlet diameter. Furthermore, in previous studies at low mass flow and low-pressure ratio, the convergent duct reduces the swirl of the flow and the radial pressure gradient close to the outlet of the computational domain and avoids convergence issues [52]. Probe sections were placed at the same location as in the experiment, as depicted in Fig. 2.

3. Simulation setup

Over the length of this paper, the flow in the vaneless space has been analyzed at eight equidistant radii from 20.51 mm to 28.30 mm and at 20%, 50%, 80% stator span as well as for the entire passage height. The selection of these locations of data acquisition is represented in Fig. 3. For the aerodynamic study of the flow in the stator regions, vaneless space, and rotor under different conditions, the CFD software Star-CCM+ 2019.1 (Build 14.02.010-R8)

Table 1
Geometrical details of the turbocharger turbine.

Stator			
Stator vane number	11		
Tip clearance	0.2 mm		
Nozzle vane height	8 mm		
Chord length	18.95 mm		
Vane angle α (VGT opening)	78.34 ° (10%)	72.94 ° (30%)	43.02 ° (100%)
Vane throat area	11.88 mm ²	21.74 mm ²	68.20 mm ²
Vless space throat area	60.48 mm ²	57.02 mm ²	23.39 mm ²
Rotor			
Inlet diameter	41 mm		
Outlet diameter	38 mm		
Blade number	9		
Outlet blade angle	59°		
Tip clearance	0.36 mm to 0.4 mm		

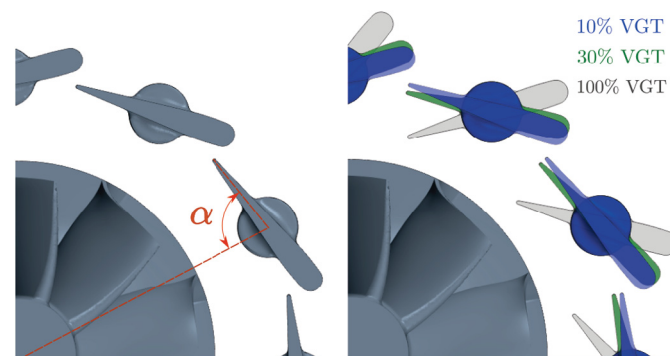


Fig. 1. Stator vane angle representation, which values correspond to the selected percentage of opening of 10% (stator vanes in blue color) and 30% (stator vanes in green color). The maximum aperture of the vanes, it means 100%, is represented in light gray color. (For interpretation of the colors in the figure(s), the reader is referred to the web version of this article.)

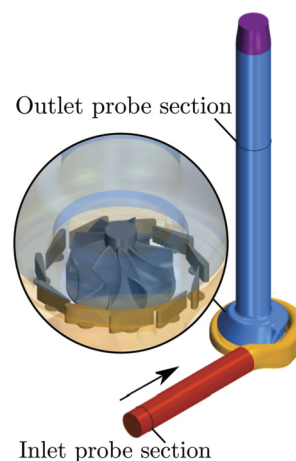


Fig. 2. Computational domain [52].

was employed. The fluid was considered an ideal and compressible gas. Since the subsonic and supersonic flow with the presence of shock waves is the approach of this research, the density-based coupled solver has been chosen [54]. This paper presents two types of simulation. First, steady Reynolds averaged Navier Stokes (RANS) simulations with a frozen rotor with mixing plane were chosen in the steady simulations to avoid vanishing of rotor-stator interactions; RANS equations are commonly used to resolve the flow in small radial turbines [55]. The second type are unsteady RANS simulations (URANS) for selected operating conditions. To model the

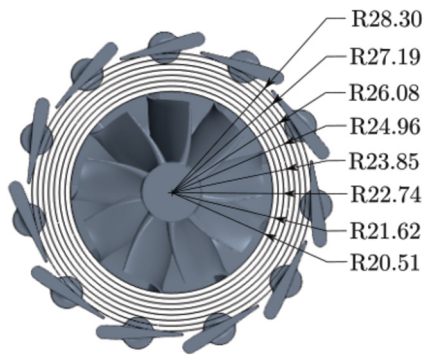
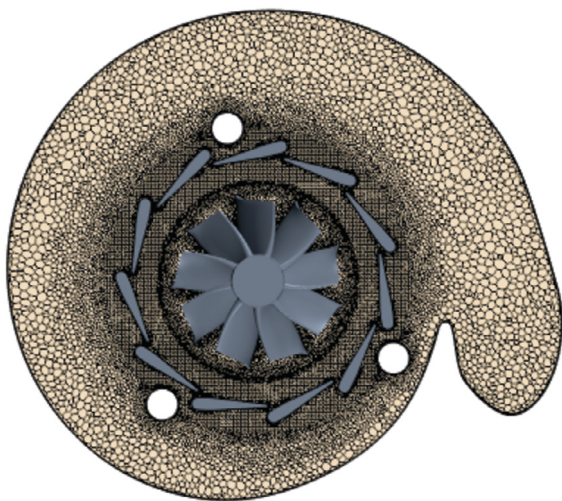
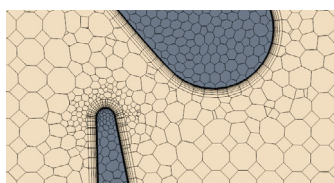


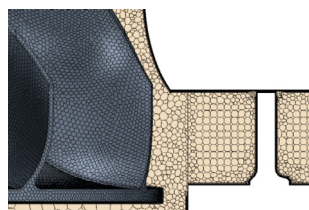
Fig. 3. Turbine geometry with highlighted sections for following analysis. Dimensions in millimeters.



(a) Front view.



(b) Stator vane.



(c) Stator throat.

Fig. 4. Utilized mesh.

effects of turbulence, the $k-\omega$ SST model [56] has been chosen, as it is widely recommended and well-validated for radial turbomachinery in the literature [37,52,57]. The fluid domains corresponding to the inlet and outlet duct have been discretized by mean of a generalized cylinder mesher to generate an extruded mesh along the duct's length, whereas an unstructured polyhedral mesh has been used for the volute, stator and rotor, as can be seen in the Fig. 4-(a). An extensive mesh sensitivity analysis was performed to achieve an adequate grid independence as depicted in Fig. 5. For the mesh analysis, the operational point with higher pressure ratio and lower rotational speed where a choked flow field with strong shock waves is expected has been simulated [16]. Furthermore, the highest mass flow rate is obtained at this operational point. This analysis was executed based on the geometries with an extremely closed position of 10% and a mostly opened VGT position of 80% using RANS simulations and a frozen rotor approach. Five differ-

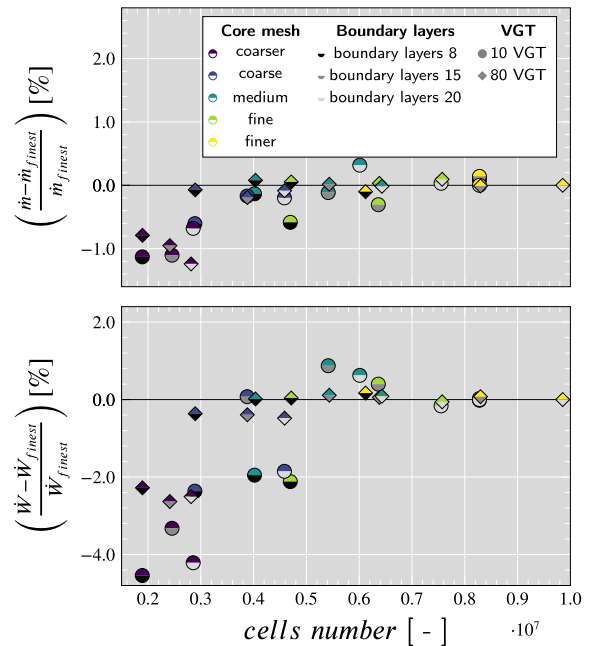


Fig. 5. Mesh analysis in turbine mass flow and turbine power for 10% VGT and 80% VGT position [16].

ent unstructured polyhedral core meshes with different densities were combined with three different boundary layer configurations of prism layer meshes. Here all boundary layer meshes are low Reynolds meshes with an y^+ -value around one. For both VGT positions, the mesh configuration owning a medium core mesh density and 15 prism layer cells close to the wall shows deficient error in mass flow and below 1% error in power extraction compared to the simulated case with the highest cell density. Thus, the choice of this mesh represents an adequate balance of obtainable numerical accuracy and computational effort. Besides of the stator vane positions of 10% VGT and 30% VGT, two reduced speeds of $3882 \text{ rpm}/\sqrt{K}$ and $8421 \text{ rpm}/\sqrt{K}$, which will be labeled from now in advance as the lower and the higher speed respectively, are selected to carry out the numerical simulations. Furthermore, the inlet total pressure is varied to achieve iso-speed lines with developing choke conditions. The flow characteristics are analyzed for two operational points of each speed line. These points have an inlet total pressure of 3.0 bar and 5.5 bar, which corresponding pressure ratios will be designated as the lower and the higher pressure ratio, respectively.

4. Results

The performance parameters considered in the current study correspond to the reduced speed, the reduced mass flow, and the isentropic efficiency total to static, defined in Equation (1) to Equation (3) respectively, where the term N is the rotational speed (in rpm) and the term π_{turb} is the total to static pressure ratio between the inlet probe section and the outlet probe section depicted in Fig. 2. In these sections, the pressure was evaluated by using mass flow averaging.

$$N_{red.} = \frac{N}{\sqrt{T_{t,in}}} \quad (1)$$

$$\dot{m}_{red.,in} = \frac{\dot{m} \cdot \sqrt{T_{t,in}}}{P_{t,in}} \quad (2)$$

Table 2
Deviation RANS and URANS simulation.

VGT	$N_{red.}$ (label)	$\pi_{turb.}$	Dev. $\dot{m}_{red.}$	$\Delta\eta_{t,s}$
[%]	$[\frac{rpm}{\sqrt{K}}]$	[-]	$[\frac{RANS-URANS}{RANS} \%]$	[% points]
10	3882 (lower)	lower	-1.63	0.91
		higher	-3.52	0.63
	8421 (higher)	lower	-3.42	2.21
		higher	-2.02	0.52
30	3882 (lower)	lower	-0.08	0.08
		higher	-0.54	0.28
	8421 (higher)	lower	2.26	0.31
		higher	-0.10	0.29

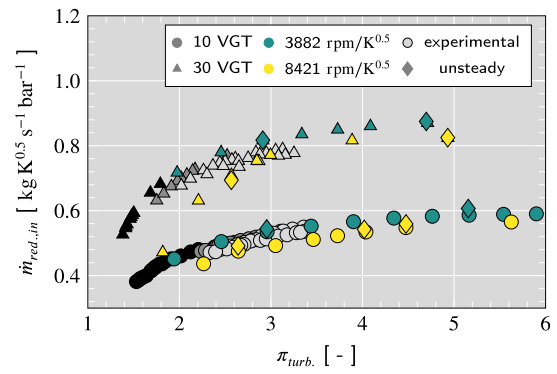
$$\eta_{t,s} = \frac{T_{t,in} - T_{t,out}}{T_{t,in} \cdot \left[1 - \left(\frac{1}{\pi_{turb.}} \right)^{\frac{\gamma-1}{\gamma}} \right]} \quad (3)$$

To evaluate the impact of the blade rotation on the turbine map parameters, the results of steady and unsteady simulations were compared, as can be seen in Table 2. For the selected operation points, the reduced mass flow presents variations up to -3.6% when the simulation is changed to unsteady conditions at 10% VGT and even less at 30% VGT, which is lower than 2.3%. Regarding the efficiency, the differences are more inferior than 2.3% and 0.31% for 10% and 30% VGT, respectively.

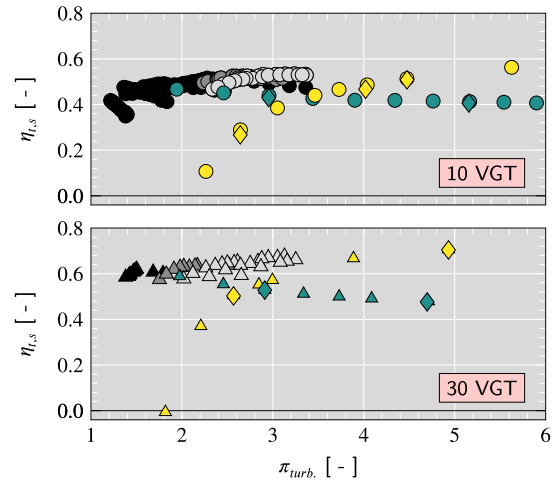
The reduced mass flow and the isentropic efficiency total-to-static at closed and partly opened position of all simulated operating points in RANS and URANS simulations are depicted in Fig. 6, along with the previous experimental results [53]. These data correspond to reduced speeds of 3882, 5830, and 7456 rpm/ \sqrt{K} at very low-pressure ratios and low mass flow. Nevertheless, the results at low speed and low-pressure ratio can be used to obtain a qualitative validation of the simulation results, as can be seen in Fig. 6 (a) in a pressure ratio range of 2.0 to 3.2. Regarding the isentropic efficiency, it is not possible to compare the simulations and experimental results directly when it is presented against the pressure ratio as depicts in Fig. 6 (b). Thus, the blade speed ratio (BSR), defined in Equation (4), is used in Fig. 6 (c) to depict the simulated efficiencies well match the experimental measurement trends. This way, for example, the higher simulated speed at 30% VGT position matches well the experimental data at higher BSRs.

$$BSR = \frac{N_{red} \cdot \pi \cdot D_{in}}{60 \cdot \sqrt{2 \cdot c_{p,turb.} \cdot \left[1 - \left(\frac{1}{\pi_{turb.}} \right)^{\frac{\gamma-1}{\gamma}} \right]}} \quad (4)$$

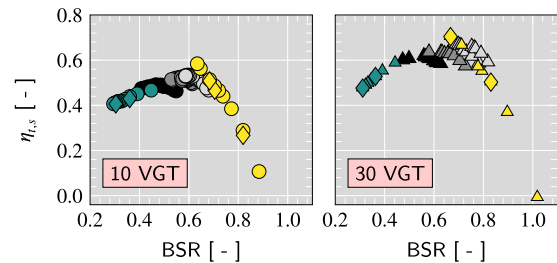
Going back to Fig. 6 (a), while the reduced mass flow stagnates at values around 0.58 kgK^{0.5}s⁻¹bar⁻¹ for 10% VGT position, the reduced mass flow reaches the choking limit at a reduced mass flow of 0.85 kgK^{0.5}s⁻¹bar⁻¹ for 30% VGT. To understand the choking mechanism in the stator and the vaneless space in more detail, the three-dimensional flow has been analyzed through the obtained CFD results. In Fig. 7 the Mach number distribution for higher and lower speed with 10% and 30% VGT opening in fully choked condition and at 50% of the span is shown. The choking area in all cases spans from the suction side of the stator vane to the rotor entry [16]. The depicted pressure profiles show an augmentation of the static pressure on the suction side due to the development of a shock wave, after which the flow decelerates, becoming subsonic. The location of the shock wave seems to be unchanged, standing at around 0.6 Rel. chord length, since the angle differs just slightly between both presented positions. Furthermore, the difference in the minimum pressure on the suction side of 10% VGT and 30% VGT opening is only 0.5 bar for a given rotational speed.



(a) REDUCED MASS FLOW MAP.



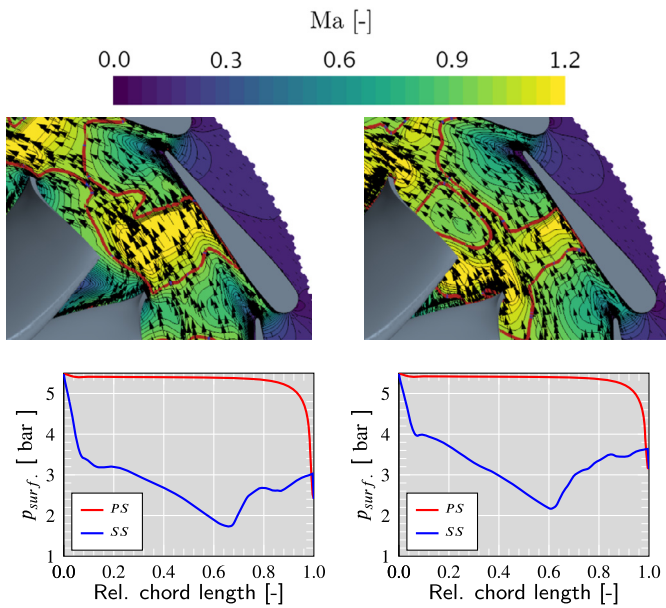
(b) EFFICIENCY VS. ER MAP.



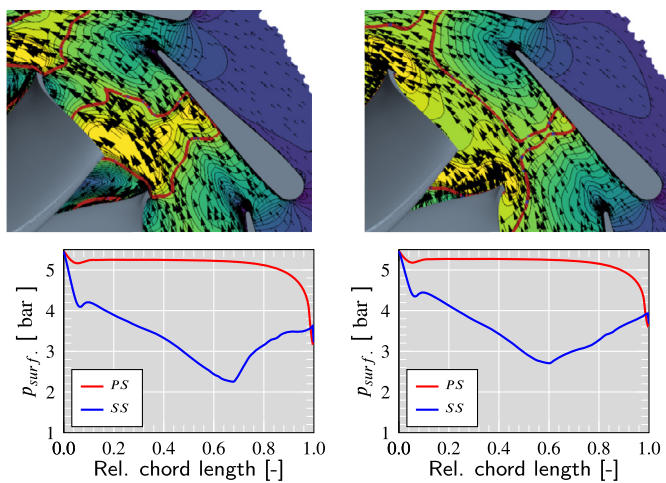
(c) EFFICIENCY VS. BSR MAP.

Fig. 6. Turbine maps based on steady and unsteady results; experimental 3882 rpm/ \sqrt{K} : black; experimental 5830 rpm/ \sqrt{K} : dark gray; experimental up to 7456 rpm/ \sqrt{K} : light gray; simulated: colored.

However, the small change in the vane angle has a considerable influence on the final choking reduced mass flow, as shown in Fig. 6 (a). Although the area between two stator vanes grows by a factor of around 1.83 (from 11.88 mm² to 21.74 mm², see Table 1), no flow with sonic speed has been identified in the throat of the stator vanes. The vaneless space throat area also changes rather less and even decreases when the stator vanes are more opened, with a factor of around 0.94 (see Table 1). While in all presented cases, a standing shock wave can be observed periodically with each stator vane in the vaneless space, at 30% VGT position and higher rotational speed, the standing shock exists only on a few stator vanes when the maximum reduced mass flow is reached. Fig. 8 shows the isosurface of the absolute Mach number equal to one. For the represented case of more opened vanes with higher



(a) Lower speed at 10% VGT opening. (b) Higher speed at 10% VGT opening.



(c) Lower speed at 30% VGT opening. (d) Higher speed at 30% VGT opening.

Fig. 7. Mach number and stator vane surface pressure profiles at 50% span of the stator passage and higher pressure ratio; red line: $Ma = 1$.

rotational speed, the reduced mass flow is slightly lower, which might cause the absence of standing shock waves and the effective choking in the vaneless space. Here, it is worth highlighting that the flow is choked in the absolute frame of reference in the inlet of the rotor. Further, the overall velocity, not the radial velocity component, is responsible for the flow choking as assumed in many one-dimensional models for choked flow in the rotor inlet. It seems that every flow particle which enters the rotor passes at least once through the isosurface. Similar to the observations made before regarding the standing shock wave on the stator vane, the flow seems to be fully choked when the flow passes only a few times through the closed surface representing the sonic limit before entering the rotor.

Using streamlines restricted to a constant stator span as depicted in Fig. 9, the theoretical flow path along a constant passage

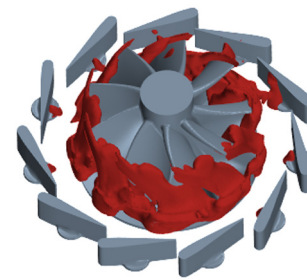


Fig. 8. Mach number with 30% VGT position for higher pressure ratio and higher speed; red surface: $Ma = 1$.

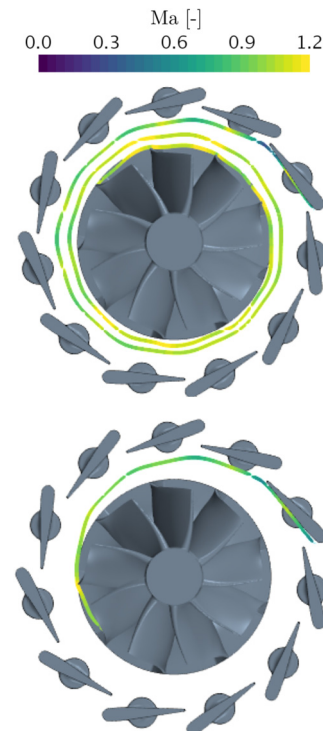


Fig. 9. Streamlines restricted to 50% span at higher pressure ratio and higher speed, describing the flow path in the vaneless space with respect to the Mach number; upper: 10% VGT opening; lower: 30% VGT opening.

height can be analyzed. Here, a restricted streamline has been chosen to reduce the impact of the starting point, which would otherwise result in the random selection of a 3D streamline. Since processed streamlines at one time step of unsteady flow results are also not representative for the flow path of a particle, results of steady RANS simulations have been used for this analysis. These results indeed lose their validity when the streamline is close to the rotor blade as the number of blade passings does not reflect the real world with a moving rotor. However, this kind of analysis can give valuable insights into the physics of the choking procedure. At a span of 50%, the least flow distortion by secondary flow phenomena was expected [58], which allows the least biased analysis of the choking mechanism. Hence, this span was selected for this analysis. The comparison of the streamlines at the choked condition at 10% and 30% VGT opening shows a significant influence on the flow path length, although the stator vane angle changes only 5.4 deg between both configurations. The flow length determines the number of stator vanes the streamline has to pass and therewith the passing of throat areas in the vaneless space. Furthermore, choking is caused as the flow passes several times through the throat between the rotor and stator vane, increasing the effective mass flow in the same throat. Hence, the area

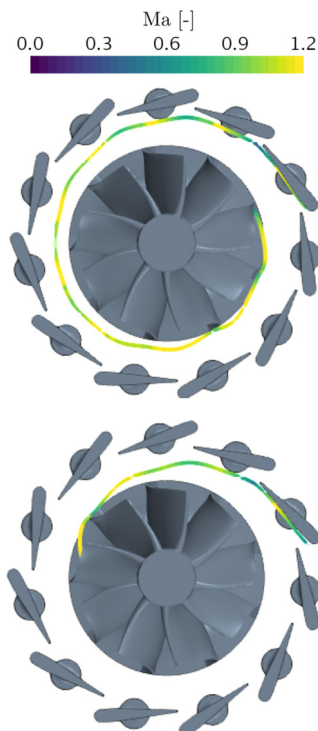
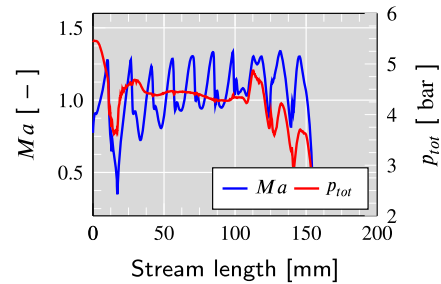


Fig. 10. Streamlines restricted to 50% span at higher pressure ratio and lower speed, describing the flow path in the vaneless space with respect to the Mach number; upper: 10% VGT opening; lower: 30% VGT opening.

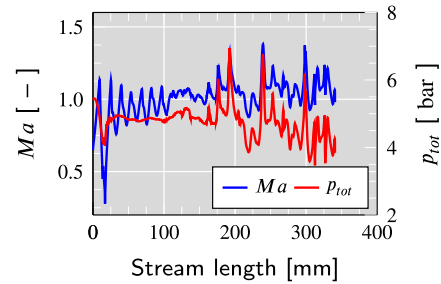
gets choked with a lower overall mass flow. This explains why the choking reduced mass flow at 30% VGT opening is around 1.5 times higher than for 10% VGT opening, although the vaneless throat area is even slightly smaller as it is shown in Table 1.

The restricted streamlines trajectory changes when the rotational speed is lower and choking condition is reached at higher pressure ratio, as shown in Fig. 10. Close to the rotor, the flow turns towards the rotor, which shortens the length of the streamline. Results presented in a later section will indicate that local shocks in the relative reference frame of the rotor are responsible for the change in direction. Considering that the choking reduced mass flow is similar to the higher speed, this might indicate that not the entire throat area between rotor inlet and stator acts as the effective choking area (from the stator vane suction side towards an effective radius upstream the rotor).

In Fig. 11 the evolution of the Mach number and total pressure along the previously presented streamlines shows the impact of both stator vane and rotor blade. Along the streamline, which passes several throats of the vaneless space, the flow experiences several accelerations above sonic speed and follows abrupt decelerations caused by shocks. Only with the first two decelerations, the total pressure shows a sudden reduction, which indicates a rather strong shock close to the suction side of the stator vane. The newly increase of the total pressure may be explained by being fed by the static pressure of the flow at higher radius newly entering the vaneless space. This way, the flow becomes newly pressurized from upstream flow in the radial direction. Furthermore, increasing total pressure might additionally be caused by the analysis of a restricted streamline at 50% span. For a VGT opening of 10%, the evolution of the total pressure and the Mach number look similar until a length of 100 mm. Before, the flow experiences seven supersonic accelerations related to passing seven throats generated by stator vanes and the rotor inlet. From that point on, the flow turning changes towards the rotor at a lower speed, while the flow turning seems to be even reduced at a higher speed. However, in

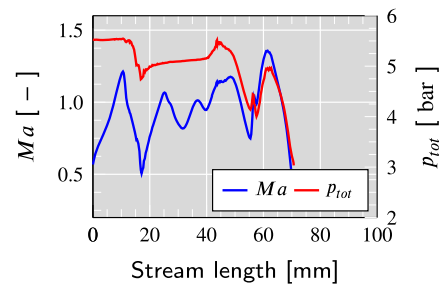


(a) Lower speed

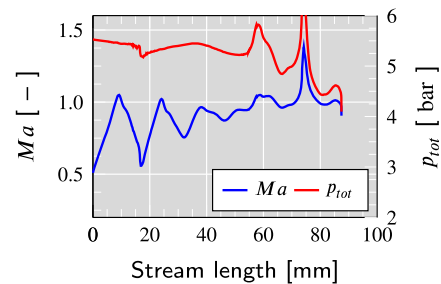


(b) Higher speed

Fig. 11. Mach number and total pressure along analyzed constrained streamlines for 10% VGT at 50% span and higher pressure ratio; upper: lower speed; lower: higher speed.



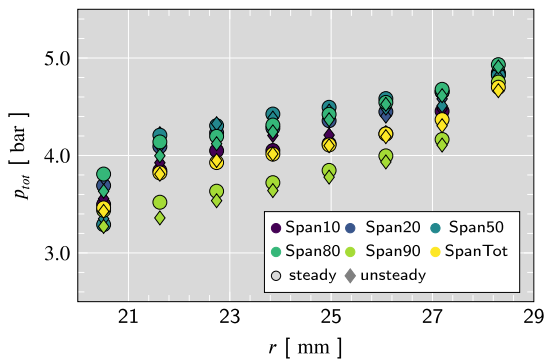
(a) Lower speed



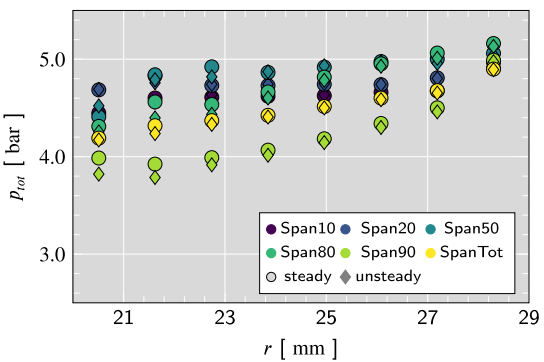
(b) Higher speed

Fig. 12. Mach number and total pressure along analyzed constrained streamlines for 30% VGT at 50% span and higher pressure ratio; upper: lower speed; lower: higher speed.

both cases, the flow appears to experience accelerations above the sonic speed now caused by the closeness of the rotor blades. While the total pressure just slightly decreases at higher speed, the total pressure is highly influenced by the rotor blades at lower speed and reduces significantly. This indicates the aforementioned shock losses caused by the rotor interaction.



(a) Lower speed

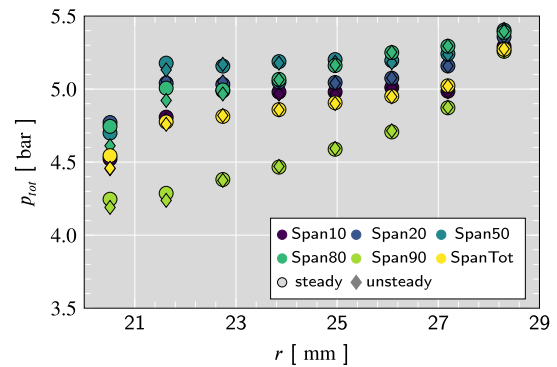


(b) Higher speed

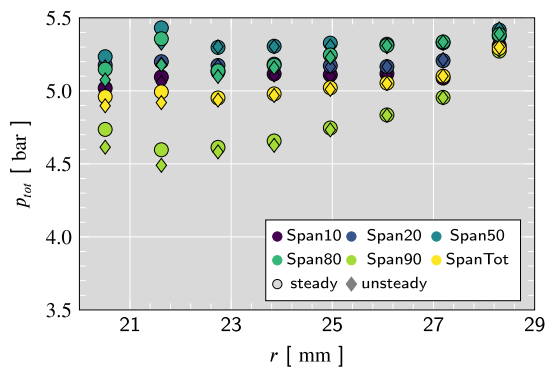
Fig. 13. Total pressure evolution in the vaneless space for 10% VGT at higher pressure ratio; upper: lower speed; lower: higher speed.

For the VGT opening of 30%, the same tendency can be observed, as is depicted in Fig. 12. The flow experiences similar accelerations and decelerations for higher and lower speed up to a flow length of 40 mm. Then the same effect occurs as observed at 10% VGT position, and the flow is turned inwards by shocks experienced in the relative reference frame close to the rotor.

To support the analysis of the restricted streamlines, the mass flow averaged total pressure at presented radii in Fig. 3 are depicted in Fig. 13 and Fig. 14 for selected spans and for the entire passage height of the vaneless space obtained by RANS and time-averaged URANS simulation results. For all spans and considering the entire passage height, the evolutions of the averaged total pressure look qualitatively similar. A significant reduction in total pressure can be observed at a higher radius, close to the stator vane. This pressure loss is caused due to the shock losses, as the streamline analysis indicated. Then the total pressure evolution towards smaller radius around the center of the vaneless space shows relatively low-pressure losses. Finally, more considerable pressure losses can be observed close to the rotor inlet at a low radius. This may be caused due to the interaction with the rotor, as the previous analysis with restricted streamlines showed. Additional pressure losses may be caused by a sudden expansion of the flow passage just before the rotor inlet. Also, the cases with lower rotational speed represent higher pressure losses close to the rotor, as the flow experiences shock losses in the relative frame of reference before entering the rotor. The growing deviation of total pressure along the spans can be explained by secondary flow phenomena as horseshoe vortices [58] and tip leakage vortices at the shroud. As previously assumed, less impact of secondary flow phenomena causes low-pressure losses at 50% span. This confirms that the choking phenomena could be mainly analyzed in the stream-



(a) Lower speed



(b) Higher speed

Fig. 14. Total pressure evolution in the vaneless space for 30% VGT at higher pressure ratio; upper: lower speed; lower: higher speed.

lines mentioned above. Further, time-averaged URANS results are very similar to the ones of steady RANS simulations for the most radial positions and spans. This shows that the previous analysis of a restricted streamline allows representative conclusions for the entire passage of the vaneless space, which are also valid when the rotor is moving. The representation of the total pressure along the vaneless space also confirms strong losses at higher radius close to the stator vane, followed by lower losses due to rather weak shocks and viscous flow phenomena at intermediate radii and significant losses close to the rotor entry.

4.1. Unsteady rotor-stator interaction

Based on the previous analysis of RANS results, it can be stated that rotor inlet and stator vanes build throats throughout the vaneless space. To assess the dynamic impact of the rotor motion on the effectively choked area and the generation of transient losses, URANS results are studied in the current section. Fig. 15 shows the relative Mach number distribution in the vaneless space. While the relative Mach number at higher speed remains clearly subsonic, the lower rotational speed allows the evolution of sonic flow close to the turbine wheel inlet. This can cause strong shocks close to the rotor leading edge when the rotor passes this region. Due to the strong shock, the flow is turned inwards, and higher losses were observed close to the rotor when the rotational speed is low. This also seems to be the origin for very low efficiencies at low speeds when the turbine is choked with very closed stator vanes. For a deeper analysis of the rotor-stator interaction, numerical Schlieren is depicted in Fig. 16 for one blade passing with both analyzed reduced speeds and both at the fully choked condition with 10% VGT opening.

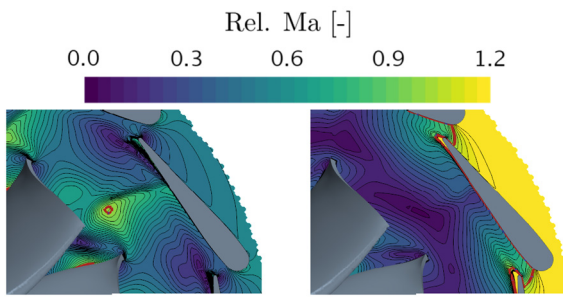
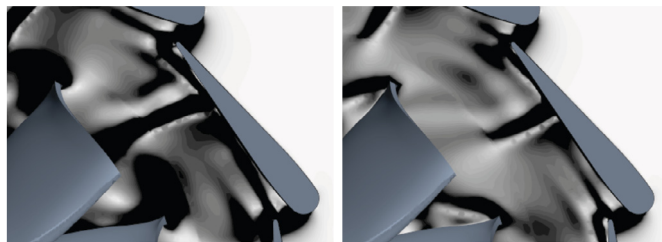
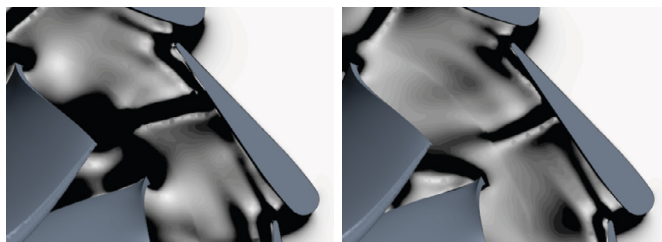


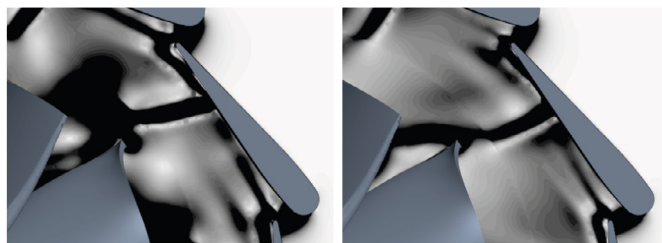
Fig. 15. Relative Mach number for 10% VGT at higher pressure ratio; left: lower speed; right: higher speed; red line: $Ma_{rel} = 1$.



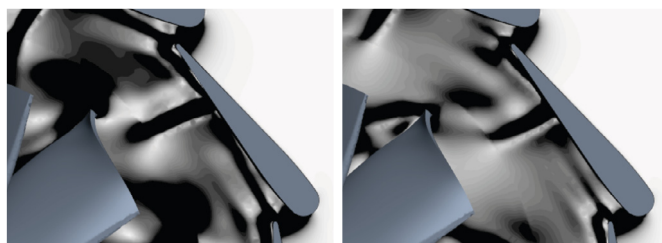
(a) $t = 25\%$ rotor blade passing.



(b) $t = 50\%$ rotor blade passing.



(c) $t = 75\%$ rotor blade passing.



(d) $t = 100\%$ rotor blade passing.

Fig. 16. Transient numerical schlieren for 10% VGT opening at 50% span of the stator passage with higher simulated pressure ratio; left side: lower speed; right side: higher speed.

The results obtained with a higher speed show negligible variations close to the stator vane, as it is shown in Fig. 16-right side. The shock at the vane suction side does not change its intensity over the entire blade passing. Although the orthogonal shock is diminishing in its intensity towards the rotor domain, the shock is extended when the rotor passes exactly the coordinates of the stator vane shock. For a short time, the rotor supports the formation of a throat, causing the extension of the shock in the absolute reference frame.

At lower speed, the stator vane shock is leaned backward and shows higher intensity in Fig. 16-left side in comparison to the previously described operating point. The higher intensity may result from operation at slightly higher reduced mass flow. In contrast to the results at higher speeds, the shock wave seems to vary its angle depending on the rotor blade position. However, independent from the rotor blade position, the shock on the stator vane has a longer extension towards the rotor. As previously concluded, the moving rotor blade encounters locally supersonic speed, resulting in the formation of shock waves in the relative frame. Those shock waves cause distortions in the pressure field downstream of the standing shock, which explains the variation in the angle of the shock wave propagating from the stator suction side. At the same time, it is to be expected that the passing rotor blade acts in the absolute frame like in the case of the higher speeds and assists in the formation of a throat. This interaction with the rotor explains the slight deviations of turbine efficiency between steady and unsteady RANS simulations. To allow more insight into the lost generation, which is needed for the development of one-dimensional loss models, the contribution of the losses of the flow just before entering into the rotor (losses at lower radius in Fig. 13) has been studied. Therefore, the Mach number and the total pressure have been extracted at several radial positions along one entire circumference and at every time step. The results for the lower speed are presented in Fig. 17. At higher radius (Fig. 17 (a) & (b)) the Mach number distribution seems to be independent of time. Here, eleven minima and maxima represent the interaction with the stator blades. However, diagonal patterns with time dependency occur closer to the rotor. Those patterns are related to the movement of the rotor blades. The slope depends on the rotational speed of the rotor. Directly in front of the rotor inlet (Fig. 17 (c) & (d)), the influence of the rotor is clearly visible, and nine minima and maxima, which equals the rotor blade number, can be identified.

These strong fluctuations are caused by the local acceleration in front of the rotor leading edge, as can be observed in Fig. 7 for all operating points. Weak shock waves may generate the loss patterns which are visible in Fig. 17 (d) - right. These shock waves seem to be continuously generated at any position of the rotor wheel. However, the intensity depends on the relative orientation to the stator vanes. Although the impact of the stator vane shock diminishes towards the rotor inlet, an explicit dependency on the shock waves close to the rotor leading edge can be identified. Islands of local maxima mark the presence of the stator vane shock. When the rotor passes this throat, the rotor blade supports the restriction of the effective throat area, causing a local acceleration in the absolute frame of reference. Due to the locally increased Mach number in the throat, the shock appears to be stronger. Additionally, the local sonic speed in the relative frame shown in Fig. 15 contributes significantly to this loss. The variation of total pressure losses shown in Fig. 17 (d) - right is related to this shock dynamic. The comparison with the results at the higher speed emphasizes the importance of the strength of the shock caused in the relative frame. In Fig. 18 maxima and minima in the Mach number are less distinguished, and total pressure losses are considerably lower. However, the diagonal pattern related to the rotor movement represents the dominant pattern and is less dependent on

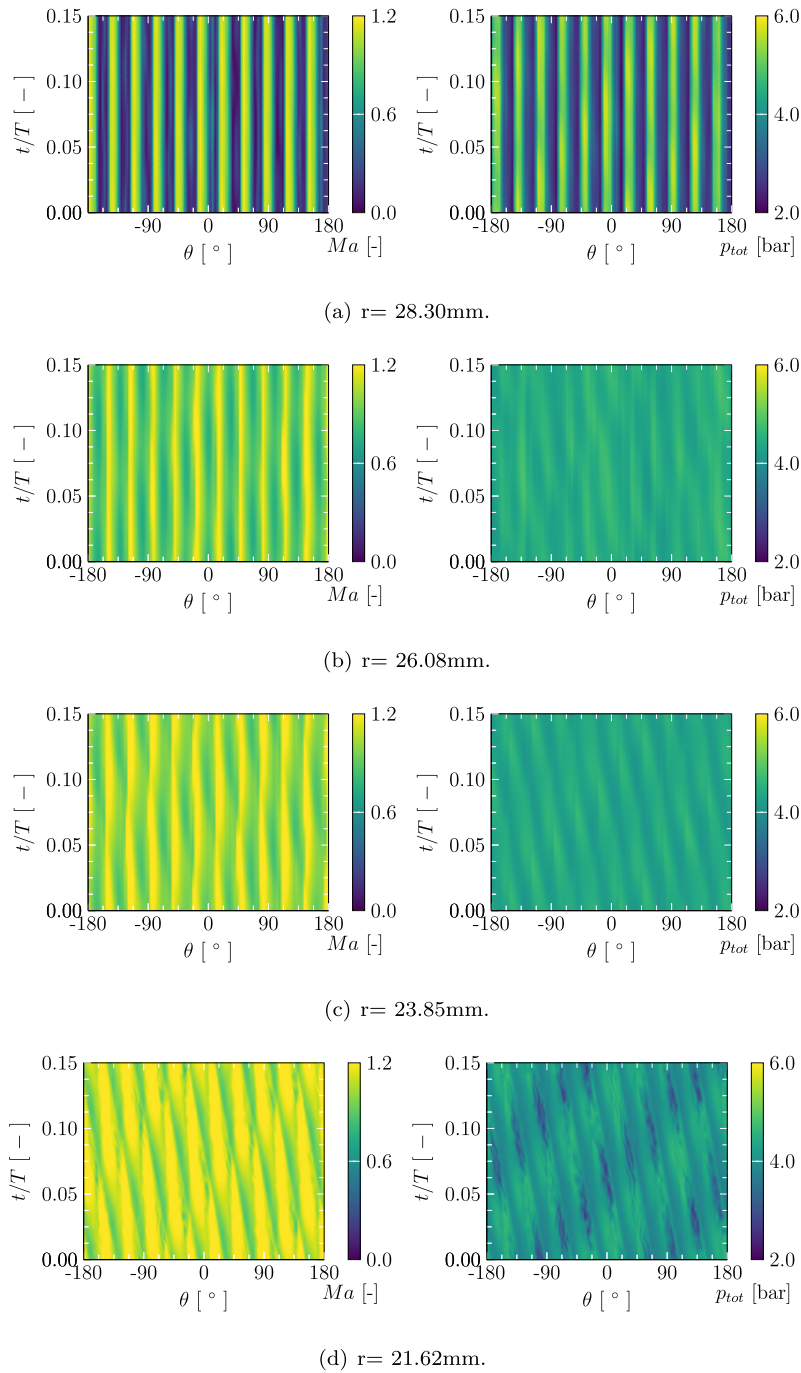


Fig. 17. Transient evolution of Mach number (left side) and total pressure (right side) for 10% VGT opening at different radial positions for higher pressure ratio and lower speed.

the stator position (due to the missing impact of shocks in the relative frame). Hence, the losses generated by the rotor in choking conditions depend on the number of rotor blades passed by a fluid particle, the flow angle, flow velocity, and rotor velocity. These parameters must then be considered in one-dimensional modeling of stator choking to estimate the generated losses adequately. Concluding, the losses close to the stator blade depend on how many times a flow particle passes the stator vane (and its choked throat with the rotor). The number of rotor blades passed by a fluid particle influences the losses close to the rotor. This accounts for low speeds where an additional shock in the relative frame generates significant losses, as well as for the higher speed where the flow has a subsonic relative Mach number. To analyze the impact of the

shock waves in the vaneless space on the rotor inlet, the transient surface pressure evolution and blade loading has been presented over time in Fig. 19. The pressure profiles seem to be less affected by the interaction with the shock front propagating from the stator SS. This might indicate that the turbine pressure profile is mostly influenced by the shock in the relative frame. At higher speed, the standing shock causes important fluctuations on both SS and PS depending on where the shock stands (SS: Fig. 16 (b); PS: Fig. 16 (d)). The fluctuations result in oscillating blade loading in the rotor inlet. The blade loading oscillates from negative to positive values every time a stator blade is passed. This might result in structural problems and material damage after longer operation in this running condition.

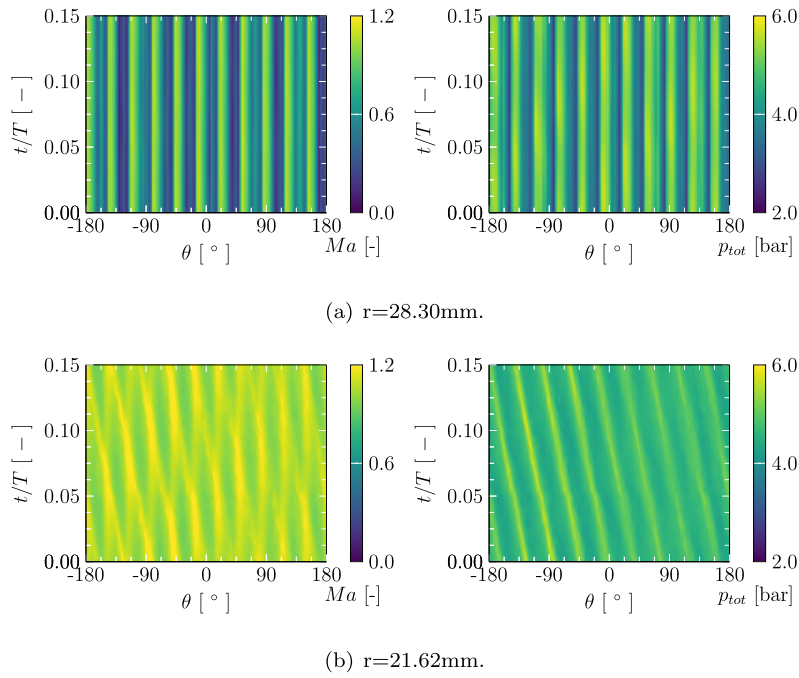


Fig. 18. Transient evolution of Mach number (left side) and total pressure (right side) for 10% VGT opening at different radial positions for higher pressure ratio and higher speed.

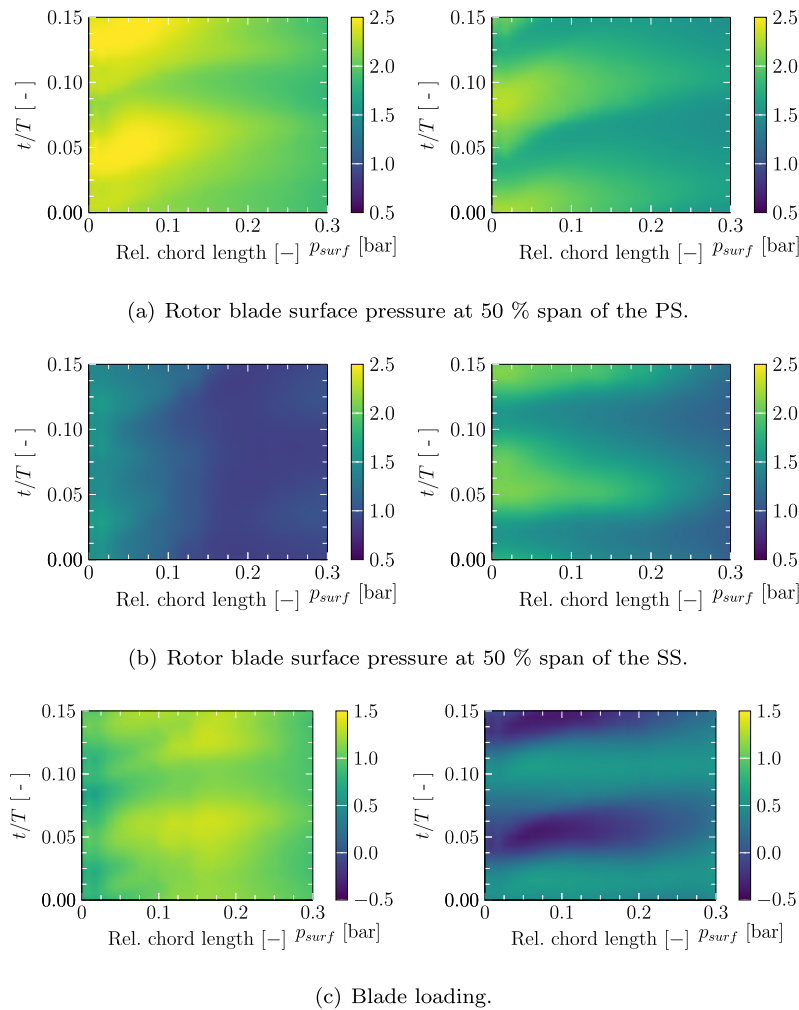


Fig. 19. Transient evolution of static pressure in the rotor for 10% VGT with higher pressure ratio at low speed (left side) and high speed (right side).

5. Conclusions

In this study, the choking in highly swirled flow in the vaneless space of a radial turbine has been characterized using RANS and URANS simulations. Instead of being effectively choked in the geometrically smallest cross-section, the high swirl causes an increase of local mass flow leading to the generation of an effective throat in the vaneless space. This throat is formed by the suction side of the stator vane and the moving rotor blades.

Following, when the variable stator vanes of a standard turbocharger turbine are at rather closed positions, a standing shock wave is developed on the suction side of the stator vane in choked condition. The effectively choked area spans from the stator suction side towards the rotor inlet at these stator vane positions. It was found that the exact location of the shock wave on the suction side varies rather with the rotational speed than with the stator vane position for the two observed VGT openings and speeds. When the rotational speed increases, the location of the shock wave slightly shifts to lower vane chord lengths.

It is essential to highlight that the shock losses are directly related to the number of shocks a fluid particle passes before entering the rotor. Close to the stator vane, the losses are significant and diminish entering the center of the vaneless space. From there, shock losses increase again, coming closer to the rotor inlet.

The rotor creates moving throats combined with the stator geometry with the same number of shock waves as rotor blades. Weak shock waves are continuously produced close to the leading edge in the absolute relative frame. These shock waves become stronger when a rotor leading edge passes the circumferential positions of the local throats. When the rotational speed is low, the relative Mach number becomes locally supersonic close to the detected throat, and additional strong shock waves are produced at the leading edge. These stronger shocks in the relative frame also turn the flow inwards, reducing the flow path. It can be assumed that this stronger shock is relevant for the pressure downstream of the shock front in the vaneless space and might influence the chordwise location towards the dependency on the rotational speed.

Rotor shock losses depend on how many times a fluid particle passes in front of a rotor blade. The shock waves can cause an alternating increase of static pressure on the pressure side and the suction side at higher speeds. The alternating pressure distribution results in oscillations of the blade loading, which might cause material failure.

At moderately closed positions (30% VGT), either the flow is choked in the rotor inlet or the stator, depending on the rotational speed.

Declaration of competing interest

The authors declare that they have no known competing financial interests or personal relationships that could have appeared to influence the work reported in this paper.

Acknowledgements

The work has been partially supported by the “Subprograma de Formación de Profesorado Universitario (FPU)”. Ministerio de Universidades. FPU18/02628 and by the “FPI Subprograma 2”. Universitat Politècnica de València. PAID-10-18.

References

- [1] T. Kawakubo, Unsteady rotor-stator interaction of a radial-inflow turbine with variable nozzle vanes, in: *Proceedings of ASME Turbo Expo 2010: Power for Land, Sea and Air*, Glasgow, UK, 2010, pp. 2075–2084.
- [2] J.G. Hawley, F.J. Wallace, A.R.J. Cox, R.W. Horrocks, G.L. Bird, Reduction of steady state NO_x levels from an automotive diesel engine using optimised VGT/EGR schedules, *SAE Tech. Pap.* 108 (1999) 1172–1184, <https://doi.org/10.4271/1999-01-0835>.
- [3] W. Bruinsicke, R. Cholvin, The turbocharger function in the light aircraft field, in: *General Aviation Aircraft Design and Operations Meeting*, Wichita, Kansas, 1964, pp. 1–9, <https://arc.aiaa.org/doi/abs/10.2514/6.1964-191>.
- [4] F.J. Jiménez-Espadafor Aguilar, J.A. Vélez Godiño, Innovative power train configurations for aircraft auxiliary power units focused on reducing carbon footprint, *Aerosp. Sci. Technol.* 106 (1270–9638) (2020) 106109, <https://doi.org/10.1016/j.ast.2020.106109>, <http://www.sciencedirect.com/science/article/pii/S1270963820307914>.
- [5] I. Jennions, F. Ali, M.E. Miguez, I.C. Escobar, Simulation of an aircraft environmental control system, *Appl. Therm. Eng.* 172 (2020) 114925, <https://doi.org/10.1016/j.applthermaleng.2020.114925>.
- [6] H. Yang, X. Zhang, C. Wang, C. Yang, Design analysis of power recovery systems for cabin exhaust air, *Proc. Eng.* 121 (1877–7058) (2015) 248–255, <https://doi.org/10.1016/j.proeng.2015.08.1065>, <http://www.sciencedirect.com/science/article/pii/S1877705815027939>.
- [7] H. Yang, X. Zhang, C. Wang, C. Yang, Experimental and theoretical study on a novel energy-saving ECS for commercial airliners, *Appl. Therm. Eng.* 127 (2017) 1372–1381, <https://doi.org/10.1016/j.applthermaleng.2017.08.043>, <http://www.sciencedirect.com/science/article/pii/S1359431117324596>.
- [8] B. Hu, C. Brace, S. Akehurst, C. Copeland, J.W. Turner, The effect of divided exhaust period for improved performance in a highly downsized turbocharged gasoline engine, in: *I.o.M. Engineers (Ed.), 11th International Conference on Turbochargers and Turbocharging*, Woodhead Publishing, Oxford, 2014, pp. 27–39, <http://www.sciencedirect.com/science/article/pii/B9780081000335500032>.
- [9] V. de Bellis, F. Bozza, S. Marelli, M. Capobianco, Experimental investigation and 1D simulation of a turbocharger compressor close to surge operation, *Int. J. Engines* 8 (4) (2015), <https://doi.org/10.4271/2015-01-1720>.
- [10] C. Carey, M. McAllister, M. Sandford, S. Richardson, S. Pierson, N. Darnton, S. Bredda, S. Akehurst, C. Brace, J. Turner, R. Pearson, N. Luard, R. Martinez-Botas, C. Copeland, M. Lewis, J. Fernandes, Extreme engine downsizing, in: *Innovations in Fuel Economy and Sustainable Road Transport*, Woodhead Publishing, 2011, pp. 135–147, <http://www.sciencedirect.com/science/article/pii/B97800857092137500127>.
- [11] J.W. Turner, A. Popplewell, S. Richardson, A.G. Lewis, S. Akehurst, C.J. Brace, S.W. Bredda, Ultra boost for economy: realizing a 60% downsized engine concept, in: *Internal Combustion Engines: Performance, Fuel Economy and Emissions*, Woodhead Publishing, London, UK, 2013, pp. 3–17, <http://www.sciencedirect.com/science/article/pii/B9781782421832500019>.
- [12] A.J. Feneley, A. Pesiridis, A.M. Andwari, Variable geometry turbocharger technologies for exhaust energy recovery and boosting—a review, *Renew. Sustain. Energy Rev.* 71 (2017) 959–975, <https://doi.org/10.1016/j.rser.2016.12.125>, <http://www.sciencedirect.com/science/article/pii/S1364032116311807>.
- [13] D. Dong, Y. Moriyoshi, J. Zhu, To improve the performance of a variable geometry turbocharged SI engine by porous material application, *Appl. Therm. Eng.* 197 (2021) 117373, <https://doi.org/10.1016/j.applthermaleng.2021.117373>.
- [14] T. Huayin, Application of Variable Geometry Turbine on Gasoline Engines and the Optimisation of Transient Behaviours, Ph.D. thesis, University of Bath, 2016, https://purehost.bath.ac.uk/ws/portalfiles/portal/187959568/Huayin_Thesis.pdf.
- [15] D. Yang, L. Cao, C. Yang, D. Lao, H. Sun, Investigations on the effect of guide vane thickness and solidity on shock and unsteady flow characteristic of VNT, *J. Mech. Sci. Technol.* 34 (6) (2020) 2423–2433, <https://doi.org/10.1007/s12206-020-0518-4>, <https://link.springer.com/article/10.1007/s12206-020-0518-4>.
- [16] A. Tiseira, L.M. Garcia-Cuevas, L.B. Inhestern, J.D. Echavarría Olaya, Numerical simulation of a radial turbine at off design conditions in presence of choked flow, in: *ASME Turbo Expo 2020: Turbomachinery Technical Conference and Exposition*, ASME, Virtual Event, 2020, pp. 1–14, <https://asme-turboexpo.secure-platform.com/a/solicitations/105/sessiongallery/5225/application/46005>.
- [17] B. Zhao, M. Qi, H. Zhang, X. Shi, Investigation on effects of shock wave on vortical wake flow in a turbine nozzle cascade, *Aerosp. Sci. Technol.* 98 (1270–9638) (2020) 105690, <https://doi.org/10.1016/j.ast.2020.105690>, <http://www.sciencedirect.com/science/article/pii/S1270963819327348>.
- [18] B. Zhao, M. Qi, H. Sun, X. Shi, C. Ma, A comprehensive analysis on the structure of groove-induced shock waves in a linear turbine, *Aerosp. Sci. Technol.* 87 (1270–9638) (2019) 331–339, <https://doi.org/10.1016/j.ast.2019.02.036>, <http://www.sciencedirect.com/science/article/pii/S1270963818320388>.
- [19] S. Mehrnia, K. Miyagawa, J. Kusaka, Y. Nakamura, Radial turbine optimization under unsteady flow using nature-inspired algorithms, *Aerosp. Sci. Technol.* 103 (1270–9638) (2020) 105903, <https://doi.org/10.1016/j.ast.2020.105903>, <http://www.sciencedirect.com/science/article/pii/S127096382030585X>.
- [20] Y. Liu, C. Ynag, M. Qi, H. Zhang, B. Zhao, Shock, Leakage flow and wake interactions in a radial turbine with, in: *Turbo Expo: Power for Land, Sea, and Air*, Düsseldorf, Germany, 2014, pp. 1–12.
- [21] H. Chen, Turbine wheel design for Garrett advanced variable geometry turbines for commercial vehicle applications, in: *B. T. t. I. C. o. T. Institution of Mechanical Engineers Combustion Engines & Fuels Group, Turbocharging (Eds.), 8th International Conference on Turbochargers and Turbocharging*, Woodhead Publishing, 2006, pp. 317–327, <http://www.sciencedirect.com/science/article/pii/B9781845691745500270>.

- [22] L. Hu, H. Sun, J. Yi, E. Curtis, A. Morelli, J. Zhang, B. Zhao, C. Yang, X. Shi, S. Liu, Investigation of Nozzle Clearance Effects on a Radial Turbine: Aerodynamic Performance and Forced Response, SAE 2013 World Congress & Exhibition, vol. 1, SAE International, Detroit, United States, 2013, pp. 1–11.
- [23] T. Heuer, M. Gugau, A. Klein, P. Ansel, An Analytical Approach to Support High Cycle Fatigue Validation for Turbocharger Turbine Stages, Turbo Expo: Power for Land, Sea, and Air, vol. 1, ASME, Berlin, Germany, 2008, pp. 723–732.
- [24] X. Shi, C. Yang, Y. Liu, S.T. Liu, B. Zhao, Numerical investigation on the high-cycle pressure fluctuation mechanism of VNT rotor, in: I.o.M. Engineers (Ed.), 11th International Conference on Turbochargers and Turbocharging, Woodhead Publishing, Oxford, 2014, pp. 411–418.
- [25] H. Kosuge, N. Yamanaka, I. Ariga, I. Watanabe, Performance of radial flow turbines under pulsating flow conditions, J. Eng. Power 98 (1) (1976) 53–59, <https://doi.org/10.1115/1.3446110>.
- [26] D. Palfreyman, R.F. Martinez-Botas, The pulsating flow field in a mixed flow turbocharger turbine: an experimental and computational study, J. Turbomach. 127 (1) (2005) 144–155, <https://doi.org/10.1115/1.1812322>.
- [27] A. Costall, R.F. Martinez-botas, D. Palfreyman, Detailed study of pulsating flow performance in a mixed flow turbocharger turbine, in: ASME Turbo Expo 2005: Power for Land, Sea, and Air, Reno Hilton, Reno Tahoe, Nevada, ASME, 2005, pp. 1415–1433.
- [28] M. Qi, X. Lei, Z. Wang, C. Ma, Investigation on the flow characteristics of a VNT turbine under pulsating flow conditions, Proc. Inst. Mech. Eng., Part D, J. Automob. Eng. 233 (2) (2019) 396–412, <https://doi.org/10.1177/0954407017744922>.
- [29] Y. Xue, M. Yang, R.F. Martinez-Botas, B. Yang, K. Deng, Unsteady performance of a mixed-flow turbine with nozzled twin-entry volute confronted by pulsating incoming flow, Aerosp. Sci. Technol. 95 (1270–9638) (2019) 105485, <https://doi.org/10.1016/j.ast.2019.105485>, <http://www.sciencedirect.com/science/article/pii/S1270963819323430>.
- [30] G. Paniagua, T. Yasa, A. De La Loma, L. Castillon, T. Coton, Unsteady strong shock interactions in a transonic turbine: experimental and numerical analysis, J. Propuls. Power 24 (4) (2008) 722–731, <https://doi.org/10.2514/1.34774>.
- [31] H. Hayami, Y. Senoo, Y.I. Hyun, M. Yamaguchi, Effects of tip clearance of nozzle vanes on performance of radial turbine rotor, J. Turbomach. 112 (1) (1990) 58–63, <https://doi.org/10.1115/1.2927421>.
- [32] A.T. Simpson, S.W. Spence, J.K. Watterson, Numerical and experimental study of the performance effects of varying vaneless space and vane solidity in radial turbine stators, J. Turbomach. 135 (3) (2013) 1–12, <https://doi.org/10.1115/1.4007525>.
- [33] X. Qiu, M.R. Anderson, N.C. Baines, Meanline modeling of radial inflow turbine with variable area nozzle, in: ASME Turbo Expo 2009: Power for Land, Sea and Air, Florida, ASME, 2009, pp. 1–7.
- [34] W. Sato, A. Yamagata, H. Hattori, A study of aerodynamic excitation forces on a radial turbine blade due to rotor-stator interaction, in: I.o.M. Engineers (Ed.), Institution of Mechanical Engineers - 11th International Conference on Turbochargers and Turbocharging, Woodhead Publishing, Oxford, 2014, pp. 389–398, <http://www.sciencedirect.com/science/article/pii/B978008100033500317>.
- [35] D. Yang, D. Lao, C. Yang, L. Hu, H. Sun, Investigations on the generation and weakening of shock wave in a radial turbine with variable guide vanes, in: ASME Turbo Expo 2016: Turbomachinery Technical Conference and Exposition 2D: Turbom, 2016, pp. 1–9.
- [36] J. Liu, W.Y. Qiao, W.H. Duan, Investigation of unsteady aerodynamic excitation on rotor blade of variable geometry turbine, Int. J. Rotating Mach. 2019 (2019) 1–13, <https://doi.org/10.1155/2019/4396546>, <https://www.hindawi.com/journals/ijrm/2019/4396546/>.
- [37] A.T. Simpson, S.W.T. Spence, J.K. Watterson, A comparison of the flow structures and losses within vanned and vaneless stators for radial turbines, J. Turbomach. 131 (3) (2009) 1–15, <https://doi.org/10.1115/1.2988493>.
- [38] A. Simpson, S.W. Spence, J. Early, A numerical and experimental study of the rotor inlet flow fields of radial turbines using vanned and vaneless stators, in: ASME Turbo Expo 2009: Power for Land, Sea, and Air, vol. 7, 2009, pp. 1385–1395.
- [39] S.W. Spence, R.S. Rosborough, D. Artt, G. McCullough, A direct performance comparison of vanned and vaneless stators for radial turbines, J. Turbomach. 129 (1) (2007) 53–61, <https://doi.org/10.1115/1.2218518>.
- [40] Variable Geometry Turbine Nozzle Design for High Expansion Ratios, Turbo Expo: Power for Land, Sea, and Air, vol. 2B, ASME, Oslo, Norway, 2018.
- [41] F. Fontaneto, T. Arts, M. Simon, P. Picot, Aerodynamic performance of an ultra-low aspect ratio centripetal turbine stator, Int. J. Turbomach. Propuls. Power (2016) 1–13, <https://doi.org/10.3390/ijtpp1010003>, <https://www.mdpi.com/2504-186X/1/1/3>.
- [42] A.C. Jones, Design and test of a small, high pressure ratio radial turbine, J. Turbomach. 118 (2) (1996) 362–370, <https://doi.org/10.1115/1.2836651>.
- [43] Effects of Inlet Conditions on the Turbine Performance of a Radial Turbine, Turbo Expo: Power for Land, Sea, and Air, vol. 6, Berlin, Germany, ASME, 2008.
- [44] M. Cerdoun, A. Ghenaïet, Unsteady behaviour of a twin entry radial turbine under engine like inlet flow conditions, Appl. Therm. Eng. 130 (2018) 93–111, <https://doi.org/10.1016/j.applthermaleng.2017.11.001>, <https://www.sciencedirect.com/science/article/pii/S1359431117308712>.
- [45] Validation and Development of Loss Models for Small Size Radial Turbines, Turbo Expo: Power for Land, Sea, and Air, vol. 7, ASME, Glasgow, UK, 2010.
- [46] H. Tamaki, S. Ouchida, M. Unno, Experimental fluid dynamics applications in radial turbomachines: inlet recirculation in centrifugal compressor, rotating stall and flow in vaneless diffuser, and improvement in accuracy of CFD for predicting flow fields in a radial turbine rotor, J. Phys. Conf. Ser. (2021) 1909, <https://doi.org/10.1088/1742-6596/1909/1/012089>, <https://doi.org/10.1088/1742-6596/1909/1/012089>.
- [47] B. Zhao, H. Sun, X. Shi, M. Qi, S. Guo, Investigation of using multi-shockwave system instead of single normal shock for improving radial inflow turbine reliability, Int. J. Heat Fluid Flow 71 (March 2018) 170–178, <https://doi.org/10.1016/j.ijheatfluidflow.2018.03.018>, <http://www.sciencedirect.com/science/article/pii/S0142727X17305507>.
- [48] F. Rubecchini, M. Marconcini, A. Arnone, A.S. Del Greco, R. Biagi, Special challenges in the CFD modeling of transonic turbo-expanders, in: ASME Turbo Expo 2013: Turbine Technical Conference and Exposition, San Antonio, Texas, USA, ASME, 2013, pp. 1–10.
- [49] J. Chauvin, A. Albrecht, G. Corde, N. Petit, Modeling and control of a diesel HCCI engine, in: Proceedings of the Fifth IFAC Symposium on Advances in Automotive Control, 2007, pp. 1–8.
- [50] M. Ammann, N.P. Fekete, L. Guzzella, A.H. Glatfelder, Model-based control of the VGT and EGR in a turbocharged common-rail diesel engine: theory and passenger car implementation, SAE Tech. Pap. 112 (2003) 527–538, <https://doi.org/10.4271/2003-01-0357>.
- [51] J. Galindo, V. Dolz, J. Monsalve-Serrano, M.A. Bernal, L. Odillard, Impacts of the exhaust gas recirculation (EGR) combined with the regeneration mode in a compression ignition diesel engine operating at cold conditions, Int. J. Eng. Res. 22 (12) (2021) 3548–3557, <https://doi.org/10.1177/14680874211013986>.
- [52] J. Serrano, R. Navarro, A. Gil, L. Inhestern, Extremely low mass flow at high blade to jet speed ratio in variable geometry radial turbines and its influence on the flow pattern: a CFD analysis, in: Proceedings of the ASME Turbo Expo, vol. 8, 2017, pp. 1–13.
- [53] J.R. Serrano, A. Tiseira, L.M. García-cuevas, L. Benjamin, H. Tartoussi, Radial turbine performance measurement under extreme off-design conditions, Energy 125 (2017) 72–84, <https://doi.org/10.1016/j.energy.2017.02.118>.
- [54] Siemens, STAR-CCM + 2019.1 release version 14.02.010-R8, <https://www.plm.automation.siemens.com/global/es/products/simcenter/STAR-CCM.html>, 2019.
- [55] M.T. Schobeiri, S. Abdelfattah, On the reliability of RANS and URANS numerical results for high-pressure turbine simulations: a benchmark experimental and numerical study on performance and interstage flow behavior of high-pressure turbines at design and off-design conditions using two, J. Turbomach. 135 (6) (2013) 1–12, <https://doi.org/10.1115/1.4024787>.
- [56] F.R. Menter, Two-equation eddy-viscosity turbulence models for engineering applications, AIAA J. 32 (8) (1994) 1598–1605, <https://doi.org/10.2514/3.12149>.
- [57] F.R. Menter, R. Langtry, T. Hansen, CFD simulation of turbomachinery flows - verification, validation and modelling, in: ECCOMAS 2004 - European Congress on Computational Methods in Applied Sciences and Engineering, July, Jyväskylä, 2004, pp. 1–14, <http://www.mit.jyu.fi/eccomas2004/proceedings/pdf/954.pdf>.
- [58] M. Alexin Putra, F. Joos, Investigation of secondary flow behavior in a radial turbine nozzle, J. Turbomach. 135 (6) (2013), <https://doi.org/10.1115/1.4024627>.